Astron. Astrophys. 323, 223–230 (1997)

ASTRONOMY
AND
ASTROPHYSICS

Numerical hydrodynamic simulations of jet-driven bipolar outflows

Michael D. Smith, Gerhard Suttner, and Harold W. Yorke

Astronomisches Institut der Universität Würzburg, Am Hubland, D-97074 Würzburg, Germany (smith, suttner, yorke@astro.uni-wuerzburg.de)

Received 21 November 1996 / Accepted 16 December 1996

Abstract. The jet model for protostellar outflows is confronted with the constraints imposed by CO spectroscopic observations. From three dimensional simulations of a dense molecular medium being penetrated by a denser molecular jet, we simulate line profiles and construct position-velocity diagrams for the (low-J) CO transitions. We find (1) the profiles imply power law variation of integrated brightness with velocity over a wide range of velocities, (2) the velocity field resembles a 'Hubble Law' and (3) a hollow-shell structure at low velocities becomes an elongated lobe at high velocities. Moreover, the leading bow shock produces strong forward motion of the cool gas rather than the expected lateral expansion. We are thus able to satisfy the Lada and Fich (1996) criteria, employing NGC 2264G as an example.

Deviations from the simple power law dependence of integrated brightness versus velocity occur at high velocities in our simulations. The curve first dips to a shallow minimum and then rises rapidly and peaks sharply. Reanalysis of the NGC 2264G and Cepheus E data confirm these predictions. We identify these two features with a jet-ambient shear layer and the jet itself.

A deeper analysis reveals that the power-law index is an indicator of the evolutionary stage: a profile steepens with time. Also, the CO excitation temperature changes along the bow walls and thus a CO line intensity does not directly yield the mass distribution, as often assumed. Instead, the CO emission is enhanced near the excitation peaks.

Key words: hydrodynamics – shock waves – ISM: jets and outflows – ISM: molecules – Infrared: interstellar: lines

1. Introduction

Molecular outflows appear at a very early stage in the life of a star. They are remarkable for their bipolarity, size and amount of out-streaming gas. In general, an outflow possesses distinct red and blue shifted lobes of gas on opposite sides of an embedded star, a length exceeding 10^6 of the size of the driving source and a mass of up to $100M_\odot$. This gas is believed to be mostly swept up and accelerated by a primary wind. As stressed by Lada and Fich (1996, hereafter LF96), how this is achieved is one of the fundamental unsolved mysteries of the outflow phenomenon. Models are based on wind-driven shells (e.g. Canto & Rodriguez 1980, Smith 1986), jet-driven bows (e.g. Masson & Chernin 1994, Chernin et al. 1994), bullet-driven bows (Norman & Silk 1979, Stone et al. 1995) and jet entrainment (e.g. Stahler 1994, Taylor & Raga 1995). However, no model has yet been able to account for the constraints imposed by observations (LF96).

We reconsider here hydrodynamic jet models. With the help of numerical simulations, we determine the direct contributions of CO emission from the jet and the bow (or, as we find, bows), as well as from the jet-cloud interaction (entrainment). Previously, we (Suttner et al. 1996, hereafter Paper 1) used these simulations to determine the nature of the propagation of a dense molecular jet into a molecular environment with densities of $10^5\,\mathrm{cm}^{-3}$ and $10^4\,\mathrm{cm}^{-3}$. We proceeded in Paper 1 to uncover the infrared signatures of the warm shocked molecular hydrogen and found a very encouraging agreement with the highly collimated, deeply embedded outflows now being discovered. One such source, NGC 2264G, has also been observed in the CO (J=2-1) millimetre line in fine detail (LF96). Such low-J CO lines have long been used to explore bipolar outflows, mapping the accumulated cold accelerated gas. Not only do we have quality data for NGC 2264G, but, because it has properties typical for a number of well collimated sources, it is an excellent candidate for direct comparison to our numerical models.

Evidence for the 'prompt entrainment' bow shock model is provided by the studies which associate shocked molecular hydrogen with the peaks of the CO outflow lobes (Davis & Eislöffel 1995). This model now appears highly plausible at least for the well collimated outflows emanating from the youngest protostars. Indeed, it would be quite convincing but for the following problem emphasized in LF96.

The high degree of bipolarity (distinct red and blue lobes) in NGC 2264G is contrary to the bow model expectations. The flanks of a bow shock should deflect stationary gas away from the observer (on the far side) as well as towards the observer, thus producing superimposed red and blue emission. Two further constraints which an acceptable model must satisfy are (1) the integrated line profiles possess power law wings and (2) the

Send offprint requests to: M.D. Smith

velocity increases with distance in a manner roughly describable as linear (see LF96).

We intend here to put our numerical work through these tests. The results from a few simulations with limited resolution cannot be used to provide the definitive answer. However, the interplay between available theory and available observations should aid in defining the problem areas and tightening constraints. In fact, the comparison made here leads us to conclude that molecular bow shocks are complex flow regions. Since bow shocks are curved shocks, vorticity is introduced into the flow which is then amplified through the enormous compression associated with molecular cooling. The creation and dissipation of the vorticity, as suggested by Smith (1994), alters the properties of the low-excitation emission.

The numerical model is described fully in Paper I. These three dimensional simulations were performed by injecting a circular jet of molecular gas of diameter 3×10^{15} cm which is allowed to drill a path out to 1.2×10^{17} cm. Dissociation and reassociation on dust, atomic and molecular cooling, and inelastic collisions of hydrogen with dust particles are included. The CO intensity has been calculated assuming statistical equilibrium and optically thin emission according to the analytic approximation obtained by McKee et al (1982). The CO density is held as a fixed fraction of the molecular hydrogen density. Since reassociation is not important in these simulations and the CO and H_2 molecules dissociate at similar shock speeds, this is a reasonable approximation. However, it should be noted that the CO abundance in the jet may differ from that in the environment, according to the relevant chemistry. We here attempt to model the J=2-1 CO line. The approximations involved, especially in dealing with gas at temperatures below 100K, must be borne in mind.

2. Results: CO line profiles

2.1. Numerical models

The CO line profiles extracted from the numerical simulations are shown in Fig. 1. We integrate over one half of a bipolar outflow with the angle to the plane of the sky α as indicated, simulating the 'red lobe' dominating side only. We find that we can ignore an inner region where some red-blue overlap at low velocities occurs, since 1) the overlap region is very small ($\lesssim$ a few jet radii) and 2) it would be difficult to distinguish this emission from the cloud background emission.

The simulated profiles possess three characteristic parts:

- a power law dependence in the low to intermediate velocity range (containing most of the emission), dominated by the leading bow shock;
- a high velocity peak at $v_j \sin\alpha$, which corresponds to the jet's direct emission;
- a dip between these two components, where the jet-bow shear layer, consisting mainly of molecules which survived the jet terminal shock, is present but rather ineffective.

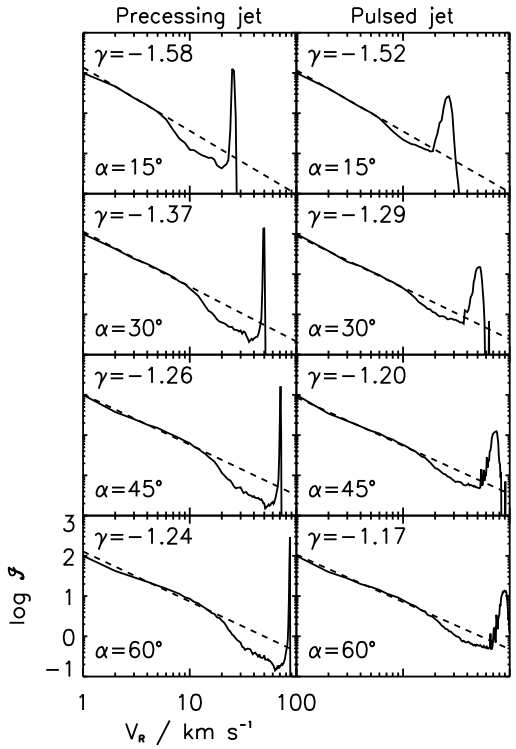

Fig. 1. Simulated CO J=2-1 line profiles from one half of a jet-driven bipolar outflow. Note the power law dependence at low velocities and the sharp peak corresponding to the jet's direct contribution. The angle to the plane of the sky α and the power law slope γ are indicated. The age is 600 years.

Note also the major differences between a pulsed and non-pulsed jet: the pulsed jet possesses a broader jet component as well as a stronger shear layer which almost fills in the dip. The pulsations, although not particularly strong in this simulation, are sufficient to cause a significant redistribution of momentum.

A quantitative analysis is provided by fitting the power law index γ, which relates the intensity to the velocity by $I \propto v^{\gamma}$. We find that γ is in the range -1.17 to -1.58, depending strongly on the viewing angle.

The jet component is extremely narrow in these simulations since the jet speed is fixed and the precession provides a limited broadening. Given the precession cone's opening angle of 1°, precession induced broadening is just $3.5\,\mathrm{km\,s^{-1}}$ for the $100\,\mathrm{km\,s^{-1}}$ jet.

We find the surprising result that the simulated lobe contains only red shifted gas. Despite the presence of a bow shock which accelerates and deflects the stationary ambient gas both towards and away from the observer, only receding gas is present in the CO outflow for a wide range of viewing angles. This phenomenon and our explanation will be discussed further in Sect. 5.1. We also find that the profile changes systematically with time. The gradual steepening of the power-law section is discussed in terms of outflow evolution in Sect. 5.2.

We have also calculated the CO line profiles for the high resolution axisymmetric runs presented in Paper 1. They are

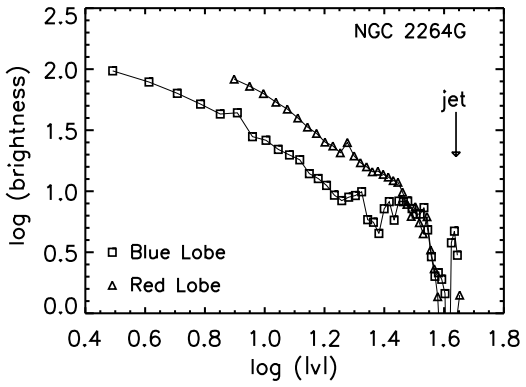

Fig. 2. Velocity profiles for the CO outflow in the red and blue shifted lobes of NGC 2264G as published by LF96 are plotted together with the additional data from their reanalysis (Lada and Fich, private comm.). The flow velocity is measured relative to the rest velocity of the outflow source.

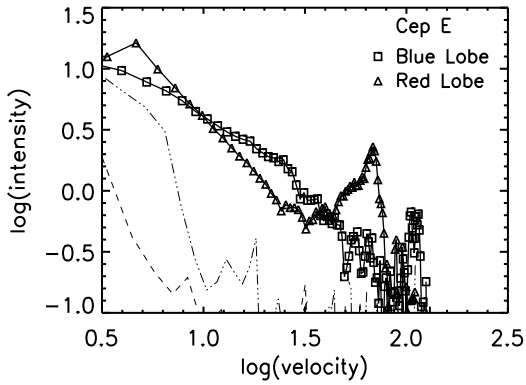

Fig. 3. The velocity profiles for the CO outflow in the red and blue shifted lobes of the Cepheus E outflow. The data is taken from Lefloch et al. (1996) and replotted in a log-log format. The dot-dashed and dashed lines without symbols represent the weak blue shifted emission from the red lobe side and the red shifted emission from the blue lobe side, respectively. Absolute velocities were recalculated relative to the background cloud (LSR velocity of -11.2 km s^{-1}).

found to possess the same properties as the profiles from the 3-D simulations, including the differences between pulsed and non-pulsed outflows.

2.2. Comparison with observations

In Figs. 2 and 3 we show recent data for two highly collimated class 0 protostellar outflows (LF96, Lefloch et al. 1996). The model components, including CO jets, are clearly visible with the following deviations. First, the jet component in the red lobe of NGC 2264 G is not easily identifiable. Secondly, the blue lobe of Cepheus E possesses several discrete clumps rather than a well defined jet, suggesting an episodic jet outflow rather than pulsations. Thirdly, the red jet is also quite broad; it may be relatively uncollimated or consist of a few components. However, Eislöffel et al. (1996) show evidence for precession with

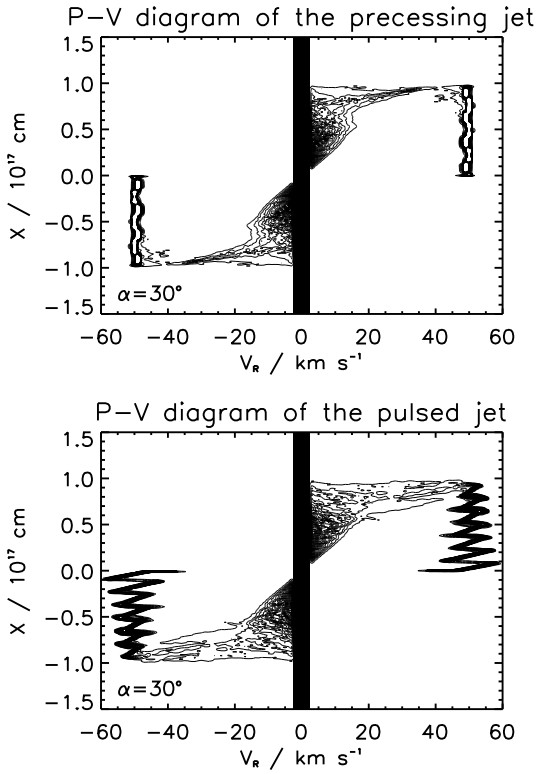

Fig. 4. Position-velocity diagrams for the CO J=2-1 line for the two models. To aid comparison with observed P-V diagrams, we plot a symmetric 'double lobe' from our single lobe simulation. Note the high velocity wiggles in the pulsed jet diagram

a precession angle of 4°. This would be sufficient to broaden the jet velocity width by 10%. Finally, the data range often does not include the low speed component, since it is veiled by the background cloud emission. However, a turnover is present in the blue lobe of NGC 2264G and the red lobe of Cep E. The corresponding shallower power law dependence is found in some of the simulations but is not so marked.

The model predictions lead us to reconsider the published data. Note that the jet component in the blue lobe of NGC 2264 G was not in the original published data, but found during a reanalysis (at our suggestion) presented by Fich & Lada (1996). It is relatively weak compared to the model predictions based on a high CO abundance. The Cepheus E data is not exactly as presented by Lefloch et al. (1996); we have altered the local standard of rest (see below) and used a log-log scale.

Many outflows demonstrate similar power law behaviour, including other class 0 protostars such as VLA 1623 ($\gamma \approx -1.83$ & -1.98, found by Andre, see Stahler 1994), L1448 ($\gamma \approx -1.4$, Bachiller et al. 1990, Tafalla 1993) and L1551 ($\gamma = -1.82$, Masson & Chernin 1992). The values lie in the range -1.3 to -1.9 (LF96). This compares quite well with the above range derived from our hydrodynamical simulations, although we did not find the steeper slopes. It would be interesting to determine if this is an evolutionary question: the simulated outflows are relatively young in real terms (600 years) as well as in geometric

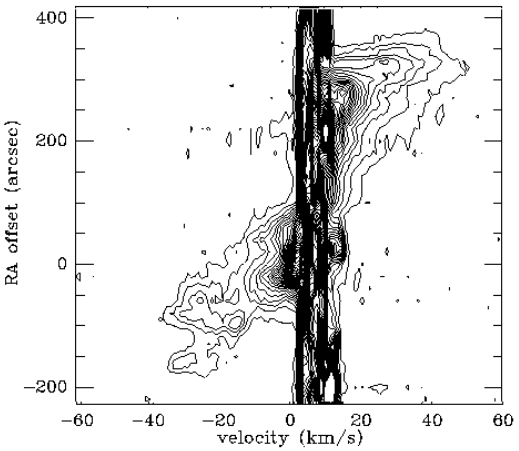

Fig. 5. Position-velocity diagram for the CO J=2-1 line for NGC 2264, reproduced with kind permission by the publisher and authors from LF96

terms (length/(jet diameter) is under 40). Older sources could develop reservoirs of slower moving gas and the slope could gradually steepen. This is explored in Sect. 5.2.

While the data for NGC 2264G yield $\gamma = -1.62 \pm 0.04$ (LF96), the data for Cep E deviates markedly: we find $\gamma = -0.96$(blue) and -2.14(red) for the LSR velocity of -13 km s^{-1} used by Lefloch et al. (1996). These values clearly lie outside the generally observed range (as well as our model range). However, the γ is sensitive to the chosen rest velocity. Hodapp and Ladd (1996) use $-11.2\ km\,s^{-1}$, and we have followed them in producing Fig. 3, and obtain $\gamma \sim -0.99$ (blue) and -1.80 (red). Had we chosen -10.0 km s^{-1} (e.g. there are superimposed clouds with various velocities), we would obtain the values -0.99 (blue) and -1.57 (red). The position-velocity diagrams of Hodapp & Ladd (1996) indeed suggest a LSR value near -10 km s^{-1}. Position-velocity diagrams from the CO observations of Lefloch et al. (1996) also indicate that the LSR velocity varies systematically across the outflow region (Lefloch, private comm.). In the model, however, we fix the background cloud to be stationary.

We also remark that there is some 'backward' motion in Cep E, as indicated by the dashed and dotted lines in Fig 3. There are several possible explanations including (1) confusion with the second larger scale CO outflow as discovered by Ladd & Hodapp (1996), (2) the result of the precession proposed by Eislöffel et al (1996) or (3) the presence of a small scale weakly-collimated wind (e.g. Cabrit & Bertout 1986, 1990). However, further observations are needed to determine if the lobes really do overlap or just result from a lack of spatial resolution.

3. Results: position-velocity diagrams

3.1. Numerical P-V models

Position-velocity (P-V) diagrams for the continuous and pulsed jets are presented in Fig. 4. We find that (a) the median velocity increases and (b) the velocity profile widens with increasing distance from the source. Furthermore, the red and blue shifted areas are spatially distinct (here we assume point symmetry with respect to the central source and display both lobes to ease comparison with the observations).

The jet may dominate P-V diagrams when (a) it contains a CO abundance comparable to the external medium and (b) the jet direction and speed do not vary greatly. One should note that a contribution from the background cloud is indicated here. This component, which dominates at velocities $\approx \pm 3$ km s^{-1}, is represented by the vertical dark stripe.

3.2. Comparison with P-V observations

The P-V diagrams for NGC 2264G is shown in Fig. 5. For bipolar outflows in general, the apparent acceleration of CO gas from the source has been known for several years (e.g. Cabrit 1993). LF96 have emphasized that this is in the form of Hubble law ie. the peak velocity increase roughly linearly with distance. As can be seen from Fig. 5, the model simulates the observations quite successfully. Although only a qualitative comparison is possible, the overall double-triangle P-V structure and the monotonous increase in velocity do give the appearance of a linear expansion.

The jet components are not apparent on the P-V diagram of NGC 2264G. This is not surprising, considering the weakness of the jets in the integrated line profile. However, for Cep E we would certainly expect to 'see' the jets on a P-V diagram and indeed they do appear in preliminary low spatial resolution data (Lefloch, priv. comm).

4. Results: CO Intensity distributions

Synthetic CO images of the non-pulsed and pulsed 3D simulations are shown side by side in Fig. 6. The emission is split up into low, medium, and high velocity ranges. This demonstrates (a) a limb-brightening or hollow-shell appearance at low velocities, (b) an elongated lobe at high velocities, and (c) an increasing collimation with increasing velocity.

All three factors are indeed often observed provided sufficient spatial resolution exists (Cabrit 1993, LF96). Here, we display in Fig. 7 NGC 2264 (from LF96). This agreement with the jet-driven bow model follows expectations, as previously analyzed by Raga & Cabrit (1993).

5. Implications

5.1. The forward motion problem

Bow shock models were not expected to be viable for the following reason. When a stationary fluid is overtaken by a bow shock, it is deflected towards the shock surface. For an axi-symmetric bow one then expects the deflection to be directly away from the bow axis in all directions (see Fig. 12 of LF96). Hence, for whatever angle to the line of sight, there should be at least some material deflected both away from and towards the observer from any single bow. In direct contradiction to this expectation

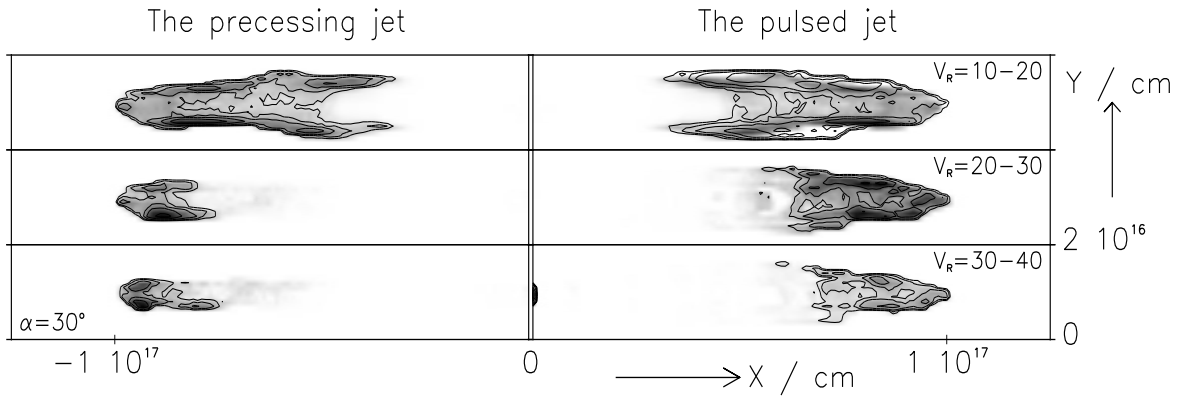

Fig. 6. Images of bipolar outflows in three velocity intervals, from 10-20 km s^{-1} (top), 20-30 km s^{-1} (middle) to 30-40 km s^{-1} (bottom). The two numerical models considered here are displayed to the left and to the right.

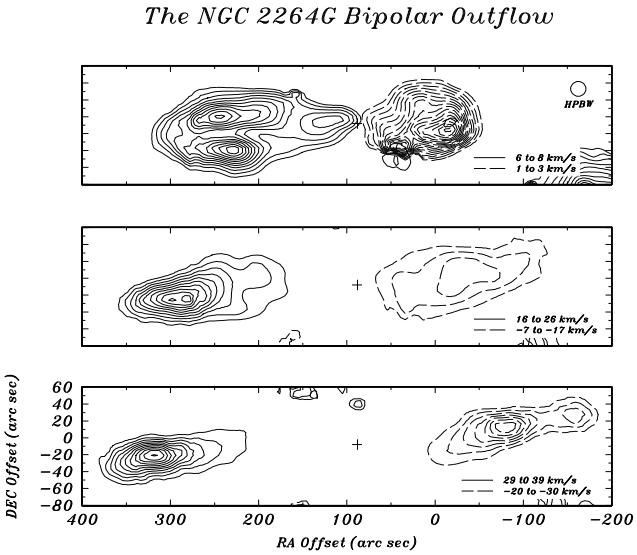

Fig. 7. Contour maps of the CO 2-1 emission from NGC 2264G in the three red (solid) and three blue shifted (dashed) velocity channels indicated. The maps were reproduced with permission by the authors and publisher from LF96 where complete details can found. At a distance of 800pc the linear size is 2.2pc. Note the non-overlapping lobes and the increasing compactness (collimation) with increasing velocity.

one finds distinct non-overlapping red and blue shifted lobes in many sources (LF96).

So how does the bow shock model manage to avoid this problem? First, we have established that the mass in a CO outflow is predominantly swept up by the bow shock. The shocked material in the wings remains molecular and cools strongly: it becomes highly compressed into a very thin layer which cannot be resolved numerically. In the present case we are unable to rigorously test the stability of this layer – this would require much higher resolution. The approximation made here is the usual one for the cooling zone behind radiative shocks (see below), where the high temperature peak can rarely be followed numerically in multidimensional simulations (e.g. Stone & Norman 1993).

Thus, what in detail could be described as an extremely thin, high vorticity shear layer is reduced to a laminar layer of the same mass flow rate and the correct mean momentum. Indeed, shear layer fluid instabilities could be expected to have exactly this effect, where the energy released heats the gas. Smith (1995) described how this energy, derived from the vorticity created in a bow shock, would enhance the columns of low-excitation molecular hydrogen levels.

Confirmation of this scenario will require extremely high resolution simulations. The dissipation of supersonic turbulence is not easy to simulate. However, in the molecular case, where the vorticity and shear across a bow may reach extreme levels, the dissipation may justifiably be treated as instantaneous.

To test if this instantaneous dissipation is sufficient to explain the strong forward motion, we have developed a simple analytical model (Appendix). We assume an axi-symmetric bow moving at an angle α away from us with strong post-shock cooling and mixing into a homogeneous layer. With this setup, strong forward motion would produce only red shifted gas. The mass flow in the layer increases as one moves from the apex to the wings. The momentum parallel to the bow surface also builds up as new fluid is added. The transverse momentum added along the bow surface goes into the centrifugal acceleration, as specified by the shape of the bow surface *a priori*. Hence, we assume high compression and simply take the post-shock speed to be exactly parallel to the bow surface.

We display the predicted radial velocity in Fig. 8. The radial velocity of the shear layer is shown as a function of the angle θ that the shock surface subtends with the bow symmetry axis. We look at the bow in the plane which contains the maximum and minimum radial velocities (ie. containing the line of sight and the bow axis). Note that $\theta = 90°$ is the apex where the radial speed is simply the radial component of the bow speed (with $\alpha = 45°$ this radial speed is $v_b \sin\alpha$). In contrast, deep into the bow wings ($\theta \rightarrow 0°$ and $\theta \rightarrow 180°$) the locally added mass and momentum must eventually dominate and the acceleration approaches zero.

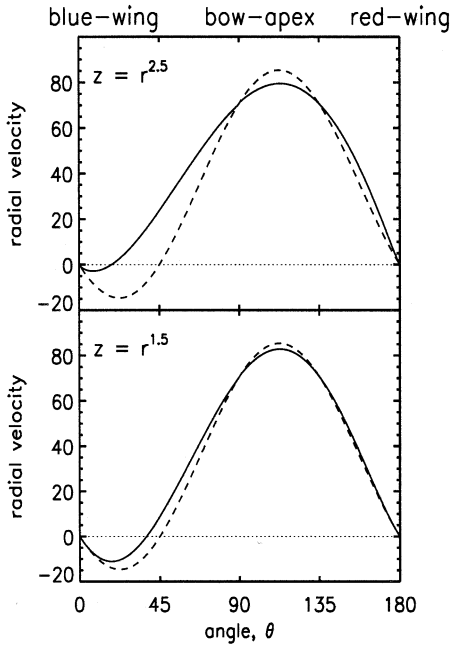

Fig. 8. Forward and backward moving gas resulting from bow shock acceleration for which the gas speed is a function only of the distance from the apex (as measured here by the angle θ of the bow surface to the flow axis). The full lines represent the observed radial velocity of a bow moving at $\alpha = 45^\circ$ to the line of sight, assuming the integrated mass and momentum in the compressed layer determine the gas speed. The dashed line is the local speed of the deflected and compressed gas, as assumed in the schematic diagram of LF96.

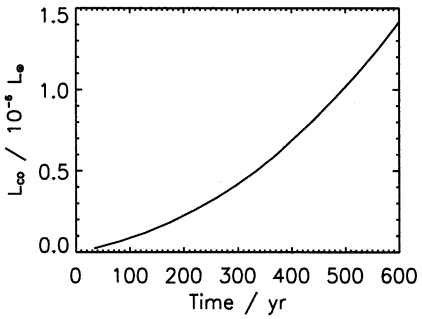

Fig. 9. The CO luminosity ratio increases systematically as a source grows. Here we show the J=2-1 integrated emission for the non-pulsed jet model.

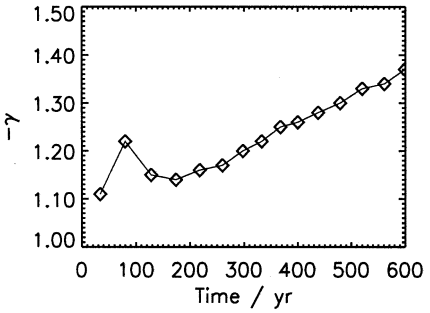

Fig. 10. The power–law index $-\gamma$ increases as the outflow grows older. Thus the line profile steepens. Here we display the index for the non-pulsed model with the orientation $\alpha = 30^\circ$.

The dashed lines in Fig. 8 represent the standard bow model: the local post-shock radial velocity is determined assuming no mixing – ie. a shear or laminar flow is maintained. The full lines represent our new analytic model for bows with a shape $z \propto r^s$ in cylindrical (r,z) coordinates (s = 2 is a paraboloid). The radial speed now depends on the bow shape. This is because the contributing amounts of momentum and mass depend on all the fluid entering the shock between the apex and the local point.

We find that the radial velocities of the gas are still not fully in forward motion. However, for $s > 2$, the 'backward motion' is confined to velocities very close to that of the background molecular cloud. These velocities cannot be observed as part of the outflow. Hence, the success of the simulations lies in the shape of the bow shocks: indeed we find that in the simulated bows the best power law approximation to the wing section yields $s = 2.4 \pm 0.1$ (although the bow is not a surface of revolution and tends to be blunter at the front (s lower) and sharper at the rear (s higher).

5.2. Evolution

The integrated CO luminosity increases steadily as more and more cool gas is accumulated, as shown in Fig. 9. However, the H_2 1-0 S(1) luminosity is fairly erratic and varies around a mean value which increases slowly with time (Suttner 1996). This is also consistent with the rapid shock production of the hot gas and the rapid cooling within about one year. Thus, it will prove difficult to employ the CO/H_2 ratio as a parameter to measure the evolutionary age of an outflow. The ratio is likely to be sensitive to other factors such as the local environment near the bow shock and the variability of the jet power.

The evolution of the CO profile power-law index γ is shown in Fig. 10. There is an initial phase which is controlled by the initial condition (ie. we begin with a blunt jet). Thereafter, the power law steepens steadily. We demonstrate in the Appendix that this is due to the gradual change in the bow shock shape. We employ the above analytical model to estimate the profile shape in the low velocity regime. This requires an approximation for the excitation temperature (proportional to the square of the absolute velocity) and to limit the analysis to the viewing angle $\alpha = 90^\circ$. The velocity and mass are then estimated as power-law functions of the angle θ, assuming instantaneous dissipation. We then find that the index gamma is related to the bow shape parameter s by $\gamma = s/2$. The result is: γ increases from 1.0 to 1.5 as the bow changes from $s = 2$ to $s = 3$. We have found that bows do indeed become more aerodynamic as they penetrate through the background cloud (Paper 1).

This demonstrative model emphasizes that the excitation temperature of the CO gas is important in determining the appearance of a bipolar outflow. This explains why CO images

exhibit peaks associated with the shock fronts as identified by the lines of relatively hot molecular hydrogen (e.g. Davis & Eislöffel 1995). Very steep profiles (which are not observed) are predicted if the excitation is assumed constant (see Appendix).

On the other hand, several sources possess $\gamma \sim 1.6 - 1.9$ (see Sect. 2). This suggests that the present simulations successfully simulate only the dynamically youngest outflows. In older outflows, we would then expect that the leading part of the bow shock is relatively blunt, but most of the CO emission arises from the extremely long flanks which form the shell of material, most of which had been entrained through the front section of the bow.

Total outflow masses are often derived from the integrated brightness of a CO emission line. In the absence of better information, the assumption is made that the excitation temperature is quite low and constant (e.g. 20 K taken by LF96). This assumption is supported by the present model since most of the observed mass lies in the low velocities where the excitation is accordingly low. Hence estimates of the total mass remain valid. Observationally, the mechanical luminosity derived from CO line emission remains difficult to estimate. For example, Davis & Eislöffel (1995) have measured the 1-0 S(1) luminosity in several CO outflow sources. They find a total H_2 luminosity of $0.12 L_\odot$ for one lobe of NGC 2264G. Given the minimum CO mechanical luminosity derived by LF96 of $0.44 L_\odot$, we find a ratio $L_{CO}/H_2 \sim 3$. By comparison, previous estimates of the mechanical luminosity yielded a ratio in the range 14-170 (Davis & Eislöffel 1995).

6. Conclusions

We have used three dimensional numerical simulations of dense molecular jets drilling through a molecular environment to determine whether a hydrodynamic model can provide a basis for discussion of the bipolar outflows from young stars. Previously we have shown that these simulations predict infrared shock structures remarkably similar to those found in highly collimated Class 0 outflows (Paper I). We find here that the correspondence is equally good for the classical CO bipolar outflows, which image the accumulated and accelerated cool gas.

We confirm that the prompt entrainment model, in which the gas traced by the observed CO molecule is mainly swept up by a leading bow shock, is able to reproduce several observed characteristics of bipolar outflows from deeply-embedded protostars. However, we are also able to identify the presence of shear layer and jet components in the hydrodynamic models.

The bow shock dilemma discussed by LF96 is that a bow deflects material both towards and away from the observer, whereas only forward motion is observed, ie. the bow appears to push material strongly in the jet direction. This problem is solved here through the impracticality of an extremely thin molecular shear layer directly behind the bow surface. The high compression caused by the molecular cooling results in a very thin, high vorticity curved stream which is unstable and which therefore cannot be maintained (e.g. Smith 1994). In the numerical simulations local mixing occurs on the scale of the grid resolution, whereby mass and momentum are conserved. In this manner shock and vorticity energy dissipation is included in our calculations. The dissipation is then responsible for maintaining the thermal excitation and thus for the shallow power-law regime of the line profiles. We are thus able to build a consistent picture. Methods to fully simulate the dissipation of supersonic turbulence behind a bow remain to be developed.

We conclude that we have successfully simulated line profiles, position-velocity diagrams, and velocity-channel images for a collimated CO outflow. This suggests that, as was the case with radio galaxies (Norman et al. 1982), a hydrodynamic jet approach is to a good extent correct. Weakly-collimated relaxed outflows are not modelled here; in such cases red and blue lobes often overlap and broader outflow models have proven to be quite successful (Cabrit & Bertout 1986, 1990).

We have been able to make a few predictions, as can be seen in Fig. 1. For example: the line structure is dependent on orientation and the jet variability. We also predict how CO jets should appear on position-velocity diagrams, something to be tested very soon. A number of questions remained unanswered, however. Are the jets themselves most often molecular and do they contain an interstellar CO abundance? How will the magnetic field alter our predictions? How are the wide outflows produced? Surely, more detailed numerical studies can help to shed light on these subjects.

Acknowledgements. We are very grateful to C. Lada, B. Lefloch and M. Fich for supplying data and figures. We sincerely thank C. Davis, J. Eislöffel, M. McCaughrean, M.-M. Mac Low and H. Zinnecker for helpful discussions. We also thank the DFG for financial support. The calculations were performed on CRAY computers at the "LRZ München", at the "HLRZ Jülich", and at the "Rechenzentrum der Universität Würzburg".

Appendix

We here present the mathematical formulation of the bow shock model discussed in section 5. We define $\tan\theta = dr/dz$. The mass flowing through the shear layer at the annulus corresponding to θ_0 is the accumulated mass inflow rate through the bow surface from the apex to this location,

$$dM/dt = \int_{\pi/2}^{\theta_0} \rho_0 v_0 \sin\,\theta\, dA \tag{1}$$

and the accumulated momentum flow rate along the bow surface is

$$dP/dt = \int_{\pi/2}^{\theta_0} \rho_0 v_0^2 \sin\,\theta \cos\,\theta\, dA \tag{2}$$

where the area dA can be written as

$$dA = \frac{L^2 d\phi d\theta}{(1-s)\cos\,\theta\,\sin^2\theta}\,[s\tan\,\theta]^{-\frac{2}{s-1}} \tag{3}$$

for a bow shape $z/L = (r/L)^s$ with ϕ the azimuthal angle. Here, ρ_0 and v_0 are the undisturbed pre-shock density and velocity.

Numerical integration yields the flow speed in the shell: $v_s = dP/dM$. Given the observation angle as defined in Sect. 2.1, $\pi/2 - \alpha$, yields the radial velocity (in the local rest frame) discussed in the text:

$$v_{rad} = v_s \cos(\theta - \alpha) - v_0 \cos \alpha. \quad (4)$$

Taking $\alpha = 90^\circ$, and θ small, we find the relationships $v = v_{rad} \propto \theta^{2/(s-1)}$, $dM/dt \propto \theta^{-2/(s-1)}$ and the length traversed by a fluid element in the shell when deflected through an angle $\delta\theta$ is $\delta L \propto \theta^{-2-1/(s-1)}\delta\theta$. Hence the total mass which possesses velocities in the interval v to $v + dv$ is $dM \propto v^{-2-s/2}dv$, which clearly yields very steep mass-velocity relationships.

The integrated brightness is proportional to the CO mass and a complex function of the excitation temperature (see Cabrit & Bertout 1990). At temperatures above $\sim 40K$, however, a linear dependence on the excitation temperature is found (LF96). Here we equate the integrated brightness I to $v^2 dM$, hence taking the excitation temperature as proportional to v^2, with turbulent dissipation providing the excitation. Note that this quantity is proportional to the available energy rather than the available mass. This gives $I \propto v^{-s/2}$. This yields the range found in the numerical work for s between 2 and 3, consistent with the shapes of the simulated bow fronts.

References

Bachiller, R., Cernicharo, J., Martín-Pintado, J., Tafalla, M., Lazareff, B., 1990, A&A 231, 174

Cabrit, S., Bertout, C., 1986, ApJ 307, 313.

Cabrit, S., Bertout, C., 1990, ApJ 348, 530.

Cabrit, S., 1993, in Stellar Jets and Bipolar Outflows, eds. L. Errico & A.A. Vittone, (Kluwer), 1.

Canto, J. & Rodriguez, L.F., 1980, ApJ 239, 982

Chernin, L., Masson, C., Gouveia Dal Pino, E. M., Benz, W., 1994, ApJ, 426, 204

Davis, C.J., Eislöffel, J., 1995, A&A, 300, 851

Eislöffel, J., Smith, M.D., Davis, C.J., Ray, T.P., 1996, AJ, 112, 2086

Fich, M., Lada, C.J., 1996, in JCMT Newsletter, March 1996

Hodapp, K.W., Ladd, E.F., 1996, ApJ, in press

Lada, C.J., Fich, M., 1996, ApJ, 459, 638 (LF96)

Ladd, E.F., Hodapp, K.-W., 1996, ApJ, in press.

Lefloch, B., Eislöffel, J., Lazareff, B., 1997, A&A in press.

Masson, C.R., Chernin, L.M., 1992, ApJ, 387, L47

Masson, C.R., Chernin, L.M., 1993, ApJ, 414, 230

McKee, C.F., Storey, J.W.V., Watson, D.M., Green, S., 1982, ApJ, 259, 647.

Norman, C.A., Silk, J., 1979, ApJ, 228, 197

Norman, M.L., Smarr, L., Winkler, K.-H.A., Smith, M.D., 1982, A&A, 113,285

Raga, A.C., Cabrit, S., 1993, A&A, 278, 267

Smith, M.D., 1986, MNRAS, 223, 57

Smith, M.D., 1994, in The physics and chemistry of interstellar molecular clouds, eds. G. Winnewisser, G.C. Pelz, Springer, Heidelberg, 318.

Stahler, S.W., 1994, ApJ, 422, 616

Stone, J.M., Norman, M.L., 1993, ApJ, 413, 210

Stone, J.M., Xu, J., Mundy, L.G., 1995, Nature, 377, 315

Suttner, G., 1996, Diplom Thesis, University of Würzburg.

Suttner, G., Smith, M.D., Yorke, H.W., Zinnecker, H., 1996, A&A, in press (Paper I).

Tafalla, M., 1993, PhD Thesis, Univ. Cal. Berkeley.

Taylor, S.D., Raga, A.C., 1995, A&A 296, 823

This article was processed by the author using Springer-Verlag LaTeX A&A style file *L-AA* version 3.